Measuring Dynamic Stiffnesses of Preloaded Distal Phalanges in Vibration - Test Bench Validation and Parameter Study

Christophe Noël*

Institut national de recherche et de sécurité (INRS), 1 rue du Morvan, CS 60027 - F-54519 Vandœuvre cedex, France

ABSTRACT

An experimental vibration test bench was built for measuring the dynamic stiffnesses and dissipated power densities of preloaded distal phalanges undergoing vibration. The aim of this test bench was to analyse the effects of vibration frequency, static preloading, and vibration excitation amplitude on local biodynamic response. Prior to implementation, the test bench was validated by comparison with a tension–compression testing machine and a reference dynamic mechanical analyser. A measurement study was then conducted on a group of 20 subjects. The mean dynamic stiffness showed that the mechanical behaviour of the index finger distal phalanx is similar to that of a complex amorphous polymer: it exhibits frequency-related stiffening with a rubbery plateau, a glassy transition zone, and a glassy state. The static preloading condition considerably modifies the dynamic response of the phalanx, as well as the dissipated power, which is significantly greater when the preloading is high. An amplitude-related softening phenomenon, similar to the Payne effect for rubber, was also revealed. This can be explained by the thixotropic character of the extracellular matrix of the distal phalanx soft tissues.

Relevance for industry: extensive exposure of the hand–arm system to regular vibration may lead to various disorders and injuries, due in part to changes in mechanical quantities, such as dynamic stress, strain, or dissipated power density, arising from the propagation of such vibration. Nowadays, the direct measurement of this biodynamic response inside soft tissues is still extremely challenging. A way to assess the overall mechanical effects of these local quantities on the human finger is to measure and analyse both the macroscopic stiffness and the dissipated power of fingers.

Keywords: hand–arm vibration, energy dissipation, Raynaud's phenomenon, phalanx dynamic stiffness, soft tissue damping

*Tel.: +33 383 50 20 00
E-mail address: christophe.noel@inrs.fr

1. Introduction

Sustained exposure to excessive vibration levels may cause a number of pathological disorders of a vascular, osteo-articular, or musculo-tendinic order (Bovenzi, 1990; Griffin, 1996; Matoba, 1994). These pathologies are generically referred to as vibration syndrome or hand–arm vibration syndrome (HAVS).

Multiple epidemiological studies (Åström et al., 2006; Chetter et al., 1997; Kattel and Fernandez, 1999; Narini et al., 1993) supported by physiological and histological observations of the acute effects of hand–arm vibration (Griffin, 2012; Krajnak et al., 2012) have shown that these disorders are partly related to the frequencies emitted by the machine held by a worker and to other co-factors, such as working posture and pushing and gripping forces.

Measurements of the biodynamic responses of the hand–arm system enable the analysis of the influence of such factors, with the aim of better understanding the mechanisms that induce these vibration disorders. For several years, multiple research studies have focused on estimating the biodynamic responses of the upper limb; most of these have involved selecting mechanical impedance (Driving Point Mechanical Impedance, DPMI) as the biodynamic response of subjects gripping a vibrating handle (Aldien et al., 2006; Burström and Lundstrom, 1998; Gurram et al., 1995; Marcotte et al., 2005). These types of measurement very often provide overall information on the hand–arm system. They are better suited to the study of bone-joint or muscle-tendon pathologies than to that of vascular disorders situated in the finger (digital) blood vessels. Therefore, in order to focus more specifically on vascular pathologies, such as Vibration White Finger or Raynaud's syndrome, it is necessary to collect accurate knowledge of the biodynamic response of finger-transmitted vibration (Griffin, 1996). There have been several attempts to obtain more local experimental data with the help of an instrumented handle by measuring, for example, the distributed impedance in the palm-fingers system (Dong et al., 2006, 2005a), or by plotting vibration transmissibility diagrams on the dorsal face of hands

(Noel, 2011). These methods are likely to accurately provide overall information on the actual use of hand-held rotary machines. However, it has proven difficult to fully determine the relative contribution of each influencing factor (contact area, push/grip forces, posture, input vibration amplitude, etc.) for a high frequency condition, and some findings even contradicted each other (Burström, 1997; Gurram et al., 1995; Marcotte et al., 2005). However, a number of studies (Adewusi et al., 2008; Dong et al., 2008a) concluded that the biodynamic responses of the hand–arm–finger system measured from instrumented handles are often subject to errors at high frequencies (> 300 Hz). Alternatively, the results are not reproducible between laboratories owing to the measuring bias introduced by the vibrating handle itself at a high frequency (producing problems of mass cancellation at high frequencies, loss of signal coherence, vibration noise related to the handle assembly, etc.). To potentially overcome the previous drawbacks, an alternative might consist of directly measuring the local biodynamic responses at the fingertips by using specific devices. For a number of years, the assessment of the local mechanical impedance of the fingers has been the objective of a number of different research fields, such as of course the pathological effects of finger-transmitted vibration (Lundström, 1984; Mann and Griffin, 1996), but also the field of human tactile sensitivity (Moore and Mundie, 1972; Moore, 1970; Wiertlewski and Hayward, 2012), the design of haptic systems (Chai-Yu and Oliver, 2005; Kern and Werthschützky, 2008), and determining mathematical models of the skin dynamic response (Gulati and Srinivasan, 1997; Hajian and Howe, 1997). The common procedure was to locally vibrate the fingertip with a small-sized probe in contact with the skin for two main phalanx boundary conditions: i) clamped fingernail (Gulati and Srinivasan, 1997; Lundström, 1984; Moore and Mundie, 1972), and ii) free fingernail (Hajian and Howe, 1997; Mann and Griffin, 1996; Wiertlewski and Hayward, 2012). When measuring the local finger biodynamic response, it was easier to carefully control the influencing parameters, such as the probe surface contact and the static-preload, than when assessing the distributed hand-finger system with an instrumented handle. The disadvantage of this method is that it does not reproduce the use of hand-held rotary machines accurately. However, at a high-frequency condition, it is reasonable to expect the trends of the biodynamic responses to be comparable for whichever test method used, because these trends reflect the mechanical behaviour of the local soft tissues, which may be weakly dependent on those of the entire hand-finger system (Wu et al., 2006). Several studies have been carried out to determine in a nearly comprehensive way the influence of a number of parameters on the local finger biodynamic response, but some of these studies have produced contradictory findings, especially regarding the preloading effect (Lundström, 1984; Moore and Mundie, 1972). Moreover, some researchers pointed out certain potential measurement inconsistencies leading to an overestimation of the inertial effects (Dong et al., 2004b; Wu et al., 2006).

The purpose of our study was to describe, validate, and use in parameter analysis form a new experimental vibration test bench for measuring the local biodynamic responses of the distal phalanx. This test bench was designed to provide accurate, reliable, reproducible results at frequencies between 20 Hz and 500 Hz. We aimed at characterizing the mechanical dynamic behaviour of fingertip soft tissues at a high-frequency (> 50 Hz) condition by reducing the effects of other disturbing factors, such as muscle activity and inertial forces produced by the bones or fingernail, as much as possible. Inertial effects were minimized by clamping the fingernail (Wu et al., 2006). To avoid muscle activity as much as possible, the static preloading was performed in a passive way by compressing the fingertip between its support and the probe instead of actively pressing the indenter by using the muscles and tendons of the finger. We first describe the experimental setup, its related metrological equipment, and the signal processing parameters. The deconvolution method for driving the electrodynamic shaker in acceleration is presented. A phase calibration procedure was applied to cancel phase mismatch due to electronic devices. The phase angle accuracy was quantified. Then, the measurement bench was validated by comparison with the results obtained from a tension–compression machine and a reference dynamic mechanical analyser. Finally, a measurement study was performed on 20 subjects. The study parameters were the vibration amplitude and quasi-static preloading. The influence of the vibration frequency on the dynamic stiffness or the mechanical power dissipated by the distal phalanx was analysed before focusing on the effects of the preloading and level of excitation vibration. These results were then examined from a rheological standpoint in an attempt to provide a number of additional physiological explanations.

2. Method

2.1. Apparatus

The experimental setup for measuring the static and dynamic stiffnesses of preloaded distal phalanges is shown in Fig. 1.

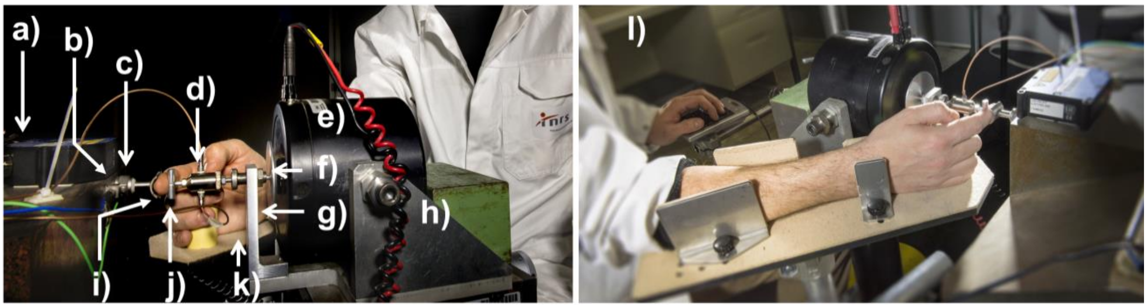

Fig. 1. Experimental apparatus: a) laser telemeter, b) control accelerometer, c) force sensor, d) impedance head, e) shaker, f) aluminium disk, g) safety arm, h) moving support, i) phalanx support, j) contact indenter, k) hand–arm rest, l) overview of the subject forearm positioning.

The seated subjects place their right forearm on an aluminium platform (Fig. 1 item k). This holder of adjustable height is fitted with four lateral stops with adjustable positions at the elbow and wrist. The purpose of these stops is to ensure appropriate positioning of the subject’s forearm and prevent intentional or unintentional movements that could potentially disrupt the measurement. The middle, ring, and little fingers grip a 30 mm diameter plastic cylinder screwed to the holder and adjustable to the subject's morphology. The index finger distal phalanx is adhered (using double sided tape) to the inside face of a curved steel support (Fig. 1 item i). This support is screwed to a piezoelectric force sensor (model B&K 8200) (Fig. 1 item c) rigidly fixed to a steel block. The force sensor is used to estimate the output effort between the fingernail and its support. A piezoelectric accelerometer (model B&K 4705B002) (Fig. 1 item b) with a low measurement range (70 m.s^{-2} sine wave peak) is positioned near the force sensor to check that the vibration level is sufficiently low so as not to disturb the output force measurement. The distal phalanx is vibrated using an electrodynamic shaker system (model B&K 4809) (Fig. 1 item e) generating a 10 to 20 kHz bandwidth signal and sustaining sine wave peak dynamic forces of a maximum of 45 N. The electrodynamic shaker is fixed to a support micrometer that is controlled manually (Fig. 1 item h). This allows the quasi-static preloading of the distal phalanx by moving the 7 mm diameter cylindrical indenter (Fig. 1 item j). The indenter is screwed to an impedance head (model B&K 8001) rigidly mounted to the vibratory shaker shaft (Fig. 1 item d). The impedance head sensor enables the measurement of both the input force applied by the cylindrical probe to the skin and the input acceleration. The compression distances used to estimate the static stiffnesses from the force/displacement curves were measured using a laser telemeter (model ILD 1700-200 from Micro-Epsilon) with a high resolution of 12 μm (Fig. 1 item a). The telemeter laser beam impacted a 4 mm thick aluminium disk (Fig. 1 item f) fixed to the shaker moving shaft.

The data acquisition, control, and computing operations were performed using MATLAB software with specific modules. A conceptual diagram of the metrological equipment with the different interconnections is shown in Fig. 2.

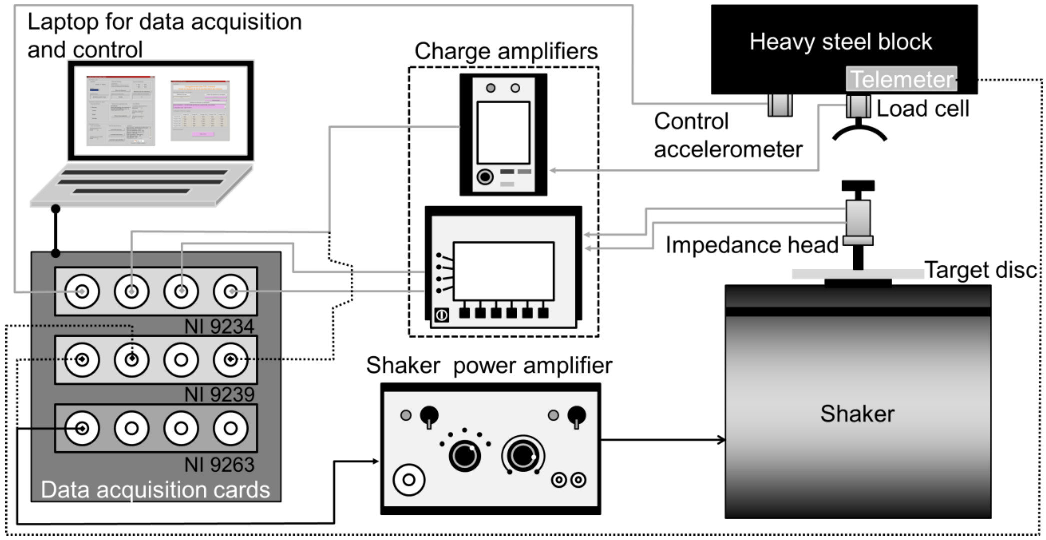

Fig. 2. Experimental test bench layout with equipment and interconnections; ⟶ source output voltage; —◆ measured on NI 9234; ⋯◆ measured on NI 9239.

2.2. Biodynamic responses

The dynamic behaviour of the distal phalanges was characterized by the input and output dynamic stiffnesses, $K_{dyn}^{Input}(\nu)$ and $K_{dyn}^{Output}(\nu)$, computed conventionally using the cross-spectrum method:

$$K_{dyn}^{Input}(\nu) = -4\pi^2\nu^2 \frac{S_{F_I,A}(\nu)}{S_{A,A}(\nu)} \tag{1}$$

$$K_{dyn}^{Output}(\nu) = -4\pi^2\nu^2 \frac{S_{F_O,A}(\nu)}{S_{A,A}(\nu)} \tag{2}$$

in which $S_{F_I,A}(\nu)$ is the cross-power spectral density between the input force $F_I(t)$ and the acceleration $A(t)$, both measured with the impedance head; $S_{F_O,A}(\nu)$ is computed from the output force $F_O(t)$ acquired with the back force sensor and acceleration $A(t)$. $S_{A,A}(\nu)$ is the power spectral density of acceleration $A(t)$. ν was the frequency and t the time. The cross-spectra and auto-spectra were calculated for a 2048 Hz sampling frequency using Welch's averaged periodogram method and Hanning windowing, a 50% overlap and a 4 Hz spectral resolution. The recorded time signal duration was 5 s. Time signal coherences were measured to ensure that their values were close to unity in the frequency band used in the study. For the input dynamic stiffness, the mass cancellation method (Håkansson and

Carlsson, 1987) was implemented in the spectral domain to overcome added mass effects induced by the indenter and the sensor seismic mass. The stiffnesses were chosen to characterize the biodynamic response instead of the more conventional mechanical impedance, because it is possible to explain the findings in the framework of experimental rheology, in which the stiffness is often used to characterize materials. This is also the reason for the output stiffness to be preferentially selected in the analysis of the findings. The fingernail was clamped so that the test bench would simulate classical rheological experimental devices as closely as possible. We therefore adopted the vocabulary used in rheology. The real part of the dynamic stiffnesses was termed the storage modulus and the imaginary part the loss modulus.

In addition to the input and output dynamic stiffnesses, the mechanical power exchanged between the cylindrical indenter and distal phalanx could be estimated. If we assume that the force exerted by the indenter on the phalanx is exerted at a point, the mean power $\mathcal{P}_{ext}$ generated by this force and applied to the distal phalanx can be conventionally expressed by frequency-based integration of the cross-spectral power density $S_{F_I,V}(\nu)$ between the force F_I and velocity V at the point of application:

$$\mathcal{P}_{ext} = \int_{-\infty}^{+\infty} S_{F_I,V}(\nu)\, d\nu \tag{3}$$

The expression shown in Eq. (3) can easily be rewritten with the input dynamic stiffness $K_{dyn}^{Input}(\nu)$ and acceleration autospectrum $S_{A,A}(\nu)$:

$$\mathcal{P}_{ext} = \int_{-\infty}^{+\infty} \left[\frac{1}{(2\pi\nu)^3} Im\left(K_{dyn}^{Input}(\nu)\right)\right] S_{A,A}(\nu)\, d\nu \tag{4}$$

In the special case of pure harmonic excitation with a frequency ν_0 and an amplitude a_0, the mean power generated by the external forces becomes:

$$\mathcal{P}_{ext} = \left[\frac{1}{(2\pi\nu_0)^3} Im\left(K_{dyn}^{Input}(\nu_0)\right)\right] \frac{{a_0}^2}{2} \tag{5}$$

Since the kinetic energy variation is zero over a vibration cycle, the mean power generated by the external forces is, in absolute terms, equal to the mean power of the internal forces. Eq. (5) thus represents the mean power dissipated by the phalanx during a vibration cycle. This dissipated power is, of course, controlled not only by the excitation amplitude, but also by the imaginary component of the input dynamic stiffness, or similarly by the real component of the input DPMI, since these two quantities are deduced from each other by division by a factor of $2\pi j\nu, j=\sqrt{-1}$. The influence of different parameters (frequency, amplitude, preloading) on energy dissipation was investigated in previous studies by the real component of the DPMI (or equivalently by the imaginary component of the stiffness) either for the local (Moore and Mundie, 1972; Wiertlewski and Hayward, 2012) or the global (Besa et al., 2007; Burström and Lundstrom, 1998) biodynamic responses of the fingers–hand–arm system. However, we introduced the so-called *acceleration power kernel* written $\mathcal{K}er(\nu)$ and expressed as:

$$\mathcal{K}er(\nu) = \frac{1}{(2\pi\nu)^3} Im\left(K_{dyn}^{Input}(\nu)\right) \tag{6}$$

for characterizing the properties of energy dissipation. The acceleration power kernel was chosen by analogy with other studies (Dong et al., 2008b, 2006), where it was used to propose a vibration-power-absorption-based weighting alternative to the existing ISO-5349 filter (ISO 5349-1:2001, 2001). Indeed, Eqs. 4 and 5 clearly show that power absorption is proportionally linked to the square of acceleration through the acceleration power kernel. As for the real component of the DPMI or the imaginary component of the stiffness, the acceleration power kernel enables the characterization of the power dissipation independently of the acceleration spectrum applied to the fingertip. However, it explains the dissipative properties of the fingertip assuming the same level of input acceleration. Based on previous studies (Dong et al., 2005c, 2004a), where a new ISO-5349 filter was proposed from the vibration power absorption density in the whole finger, we could use the acceleration power kernel measured locally at the fingertip as a new candidate for ISO-5349 weighting under high frequency.

2.3. Generation of required target input acceleration

The shaker and its power amplifier (Fig. 2) were assumed to behave as a linear system characterized by impulse response $h(t)$ between voltage $V(t)$ and acceleration $A(t)$. The aim was to establish a method of computing the voltage $V(t)$ that would produce the required target acceleration $A(t)$ at the system output. To solve this problem, we implemented a filtering method based on a restricted least squares regression, also termed the regularization method (Norcross, 2009). The Tikhonov regularization method was applied to compute the voltage $\tilde{V}(t)$, which is expressed as:

$$\tilde{V}(t) = \arg \min_{V(t)} \{\|A(t) - h(t) * V(t)\|^2 + \lambda\|c(t) * h(t)\|^2\} \quad (7)$$

in which arg min is the argument of the minimum, $\|.\|$ is the Euclidean standard, λ is a positive scalar parameter, and $c(t)$ is a function to be defined.

Fig. 3 illustrates an example of implementation of this methodology and shows the measured acceleration generated by the shaker input voltage computed from the desired target acceleration. The *rms* acceleration measured in this way was 10.3 m.s^{-2}, which closely approximated the expected value (10 m.s^{-2}).

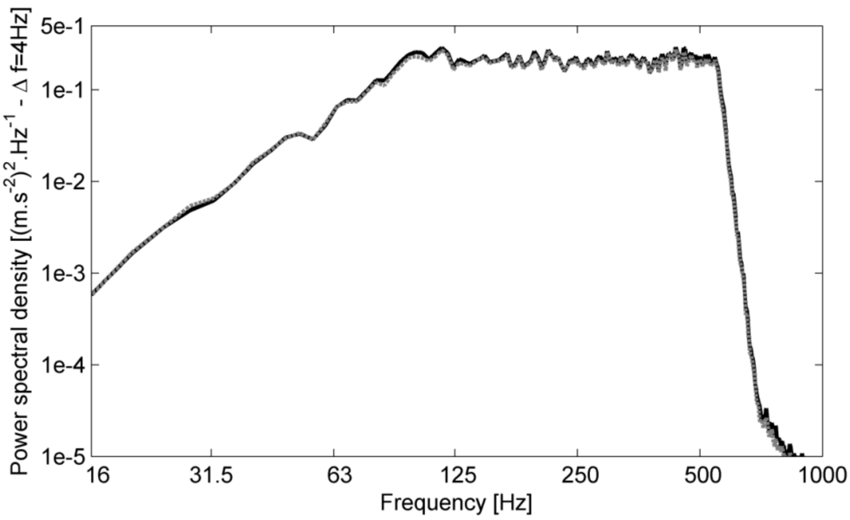

Fig. 3. Power spectral density of input acceleration transmitted by the cylinder indenter to the phalanx; - - - - 10 m.s^{-2} rms target acceleration; —— measured acceleration (10.3 m.s^{-2} rms) generated by shaker input voltage computed from desired target acceleration.

2.4. Phase angle measurement accuracy

To minimize the measurement errors of both the complex dynamic stiffness and mechanical dissipated power, it is necessary to reduce the phase angle mismatch generated by the acquisition system by as much as possible. These phase angle errors are linked to the sensors (negligible in this case owing to the high resonance frequency of the sensors), the channel-to-channel phase mismatch of the input acquisition module, and the phase shift caused by the charge amplifiers (intrinsic electronic, digital, or analogue filtering, etc.). The phase calibration was a two-step procedure (Fig. 4) consisting of: i) measuring the channel-to-channel phase mismatch, and ii) evaluating the phase shift of the charge amplifier by using a standard capacitor to simulate an ideal charge input.

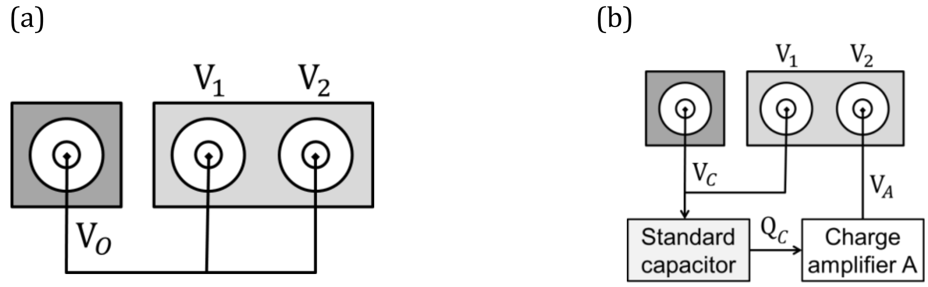

Fig. 4. Sketches showing procedure used for system phase recalibration: (a) channel-to-channel phase angle mismatch measurement; (b) phase angle mismatch of charge amplifier measurement.

To verify the phase angle adjustment procedure, the output stiffness phase angle $K_{dyn}^{Output}(\nu)$ was measured for a steel spring. Given the very low damping of this type of steel spring, its dynamic stiffness phase angle should be virtually zero. To ensure the correct positioning of the spring, the phalanx support was replaced by a flat support and the cylindrical indenter by a disk-shaped indenter. The graph of the dynamic stiffness phase angle $K_{dyn}^{Output}(\nu)$ obtained for our INRS (*Institut national de recherche et de sécurité*) test bench spring compared to that of a theoretical spring is shown in Fig. 5. As shown in the figure, it remains confined within a ± 2° band. Other measurements were taken for different springs, which provided similar results (Noel, 2015).

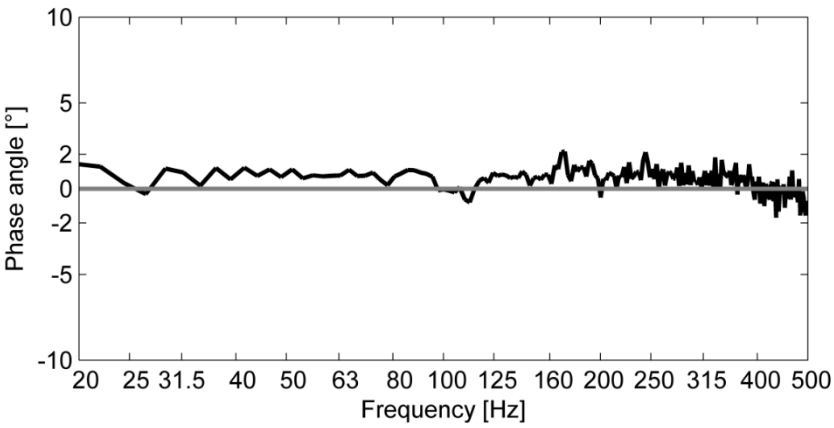

Fig. 5. Phase angle of dynamic output stiffness for control spring; INRS test bench; theoretical spring.

2.5. Test bench validation

To validate the measurements of the static and dynamic stiffnesses, the INRS test bench results were compared with those provided by reference experimental systems: a quasi-static tension–compression machine (Wolpert Testatron 20 TTZ) and a viscoanalyzer (Metravib VA 2000). The tested sample comprised a 15 mm diameter, 14 cm high polyurethane foam cylinder with mechanical characteristics approximating those of the index finger phalanx. Tests were conducted using the tension–compression machine at a displacement speed of 1 mm.min^{-1} (quasi-static load can be considered). The force-displacement curves subsequently obtained are shown in Fig. 6. The two force-displacement curves exhibited similar shapes. The INRS test bench results were higher than those obtained from the reference tension–compression machine from a compression of 1 mm upwards. The relative error between these two measurements was 9.2%, 6.5%, and 8.5% at compressions of 2 mm, 4 mm, and 6 mm, respectively. The difference between the two devices was linked to the fact that, for the tension–compression machine, the compression speed was very low (it can be considered to exhibit quasi-static behaviour), while for the INRS test bench, the compression speed ranged between 20 and 40 mm.min^{-1} (caused by the time taken by the experimenter to compress the finger). Therefore, because of the relaxation phenomena associated with the viscoelasticity properties of the finger and the higher compression speed of the INRS test bench than that of the tension–compression machine, the stress measured did not reach its quasi-static low limit. This could explain why the force–displacement curves measured with the two different devices were not identical.

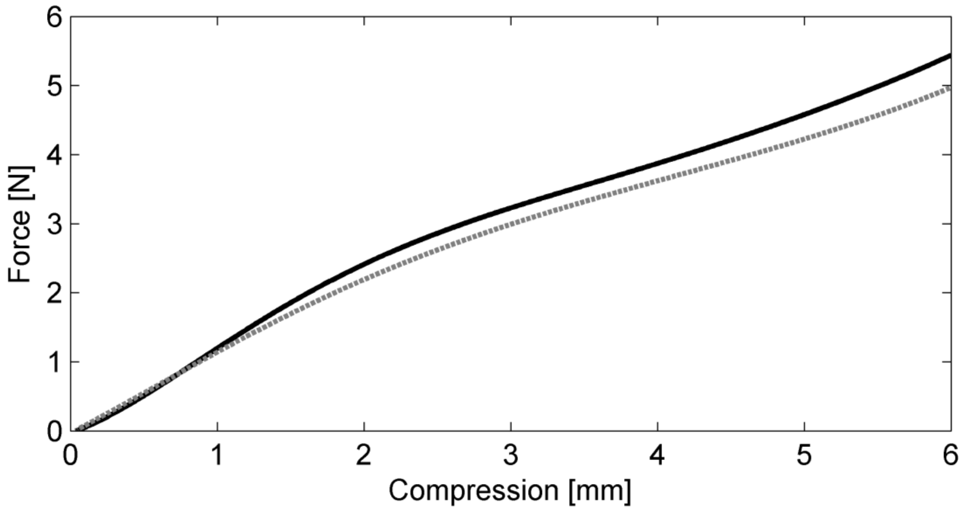

Fig. 6. Quasistatic test bench validation: force versus displacement of reference polyurethane foam sample; INRS test bench; reference tension–compression machine.

The dynamic stiffness of the polyurethane foam was then measured using a commercial viscoanalyzer. The material had previously been preloaded at a 15% compression ratio (ratio of compressed length to initial length), then vibrated by a sine wavefront generated in 10 Hz increments between 20 and 100 Hz. This viscoanalyzer was coupled with a 0.5 mm constant displacement at 9 frequencies. Measurements were taken under strictly the same experimental configurations as those of the INRS test bench. The increase in dynamic stiffness measured with these two metrological systems is shown in Fig. 7 (a). As shown in the figure, the increase of the dynamic stiffness with respect to the frequency is consistent for the two test benches. The stiffness plateau at 50 Hz, 60 Hz, and 70 Hz is visible on both curves. The relative difference between the measurements was of the order of 5%. The phase angle curves of these two sets of dynamic stiffnesses are shown in Fig. 7 (b). As shown with the dynamic stiffness, the general shapes of the two curves were similar and the relative error between the two phase angles remained below 6%. In conclusion, the INRS test bench is a reliable and accurate experimental setup enabling the measurement of the dynamic stiffnesses of preloaded phalanges in terms of both magnitude and phase angle.

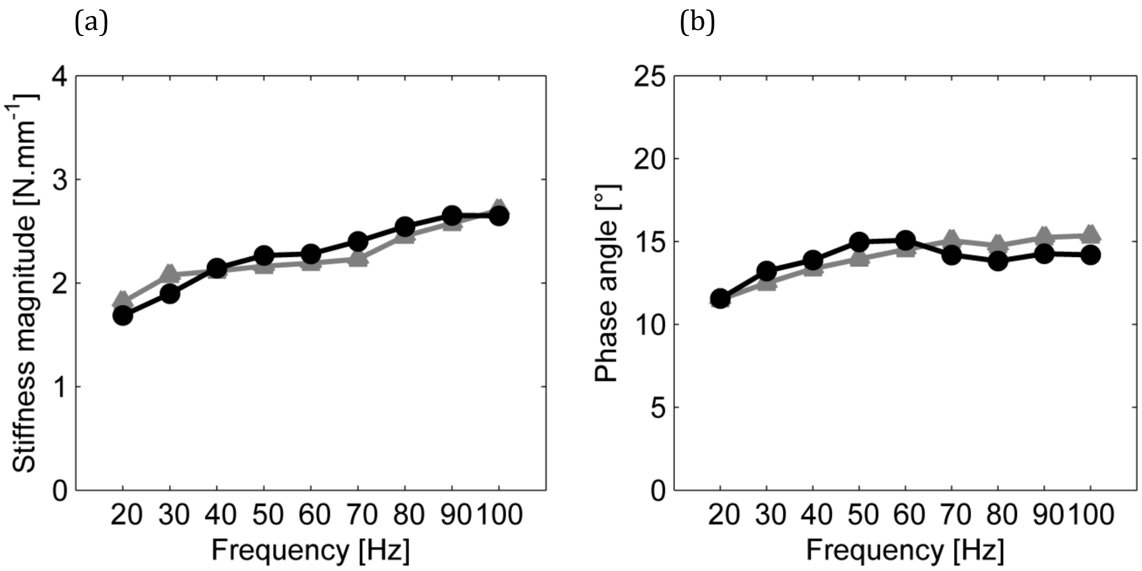

Fig. 7. Dynamic test bench validation: (a) dynamic stiffness magnitude of reference polyurethane foam sample; (b) phase angle of reference polyurethane foam sample; with INRS test bench; with commercial dynamic mechanical tester.

3. Subjects and experimental set-up

In accordance with the French law, the study protocol was reviewed and approved by the French state organism allowing biomedical research on human subjects.

3.1. Description of subject cohort

Static and dynamic stiffnesses were measured on 20 healthy, non-smoking, subjects (8 women and 12 men) aged between 19 and 39 years, and with a normal skin sensitivity threshold for their age (monofilament size 3.61 in Semmes-Weinstein test). Their distal phalanx thicknesses were measured using the laser telemeter (Fig. 1 item a). Their distal phalanx widths and index finger lengths were measured from three-dimensional images obtained by scanning each subject's hand with a laser scanner. Anthropometric markers common to all subjects and easily identifiable on these images were established in order to standardize the dimensional measurement. The distal phalanx width was defined as the width in the frontal plane (parallel to the palm of the hand) of the distal interphalangeal joint, and the index finger length was defined as the distance between the end of the finger and the metacarpophalangeal joint. The forearm volume was evaluated by simply measuring the quantity of water displaced when the subject placed his/her forearm up to the elbow in a water-filled container. Table 1 summarizes the different average anthropometric characteristics recorded for the subjects.

Table 1

Overall and forefinger specific anthropometric characteristics for cohort subjects; μ = mean and σ = standard deviation; BMI = Body Mass Index.

	Overall characteristics					Forefinger characteristics		
	Age [year]	Size [m]	Weight [kg]	BMI [-]	Forearm volume [l]	Distal Phalanx Thickness [mm]	Distal Phalanx Width [mm]	Index Finger Length [mm]
μ	22.9	1.7	66.3	22.4	1.2	13.5	17.2	78.1
σ	5.5	0.1	8.4	2.6	0.3	1.5	1.5	5.5

3.2. Experimental procedure

The quasi-static stiffnesses were computed as the derivatives of the output forces F_O with respect to the cylindrical indenter displacements measured with the laser telemeter. The dynamic stiffnesses (Eq. (1) and Eq. (2)) were estimated for the following two experimental parameters: the *rms* values of the cylindrical indenter input acceleration and the quasi-static preloading. The input accelerations were generated as described in Section 2.3. Their spectral shape is shown in Fig. 3 and their *rms* values are listed in Table 2.

The static preloading state can generally be defined in a variety of ways, such as: i) the cylindrical probe iso-displacement, ii) the iso-force applied by the probe on the fingertip (this is the definition most often selected in other studies (Dong et al., 2005b; Lundström, 1984; Lundström and Burström, 1989)), and iii) the iso-compression rate relative to the fingertip thickness. The methods that would involve specifying the preloading in relation to absolute compressions or forces were not selected, because a similar compression or force would produce, in two different subjects, two distinct forces or compressions, whose difference was not necessarily due to variations in mechanical properties, but to initial geometrical differences. For example, an 18 mm thick phalanx compressed by 3 mm would not be in the same static preloading state as a similarly compressed 11 mm thick phalanx. Moreover, a level of preloading expressed as a degree of compression with respect to the total phalanx thickness again would not define a reference state of preloading common to all subjects (for a given fingertip thickness, the flesh and bone thicknesses could be different for different subjects). Therefore, as the reference state of preloading we adopted the operating points (x_i, F_i) on the force F_i – displacement x_i curve, which provided the same static stiffness for all subjects i. The static stiffness is the macroscopic resultant of the load and deformation fields. Hence, we considered it a relevant indicator for defining a reference state of preloading. We could therefore compare the dynamic stiffnesses measured for each subject for an equivalent static load in an iso-stiffness sense.

Table 2 summarizes the 20 parameters (5 accelerations × 4 states of preloading) used for the dynamic stiffness measurements.

Table 2

Summary of setup parameters used for the dynamic stiffness measurements.

Indenter shape and dimensions	Acceleration level [m.s^{-2} *rms*]					Quasi-static stiffness [N.mm^{-1}]			
Cylinder with diameter of 7 mm	2	5	10	15	20	2	5	8	10

4. Results

4.1. Static stiffness

We plotted static stiffnesses as a function of compression for five subjects in Fig. 8 (the two extremes and three other representatives—the curves of the other subjects are similar but are not shown for a better visualization). The static stiffness curves for all subjects have the same general shape that can be divided into two main parts. At low compression, the stiffness is small with a low slope. Beyond a compression of 2.5–3.5 mm, the stiffness increases quickly with higher compression values. This behaviour is similar to that observed in certain elastomers or some polyurethane cellular foams (Riande et al., 2000). The results of the present study are in good agreement with those reported in other works (Serina et al., 1997; Wu et al., 2003) in which high dispersion existed over the subjects and the stiffness had the same order of magnitude.

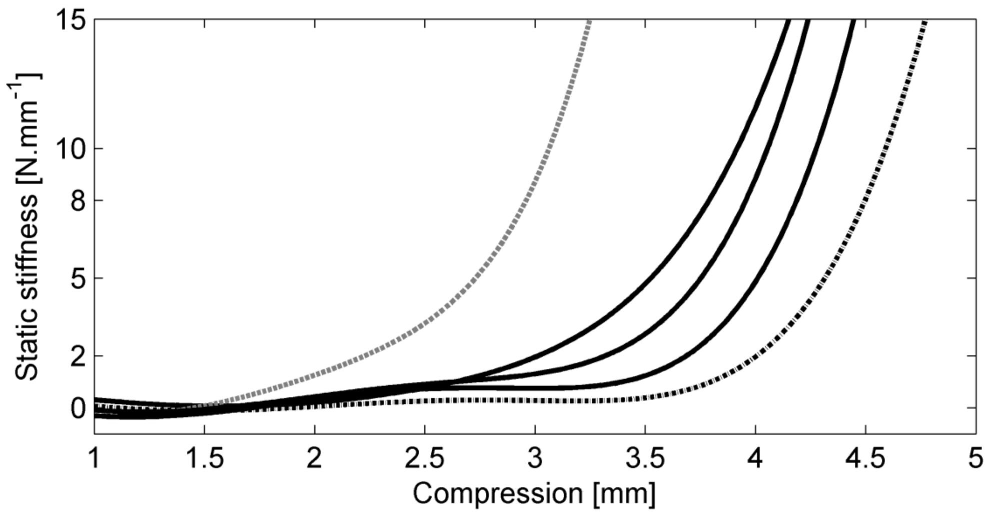

Fig. 8. Example of static stiffness for five subjects; - - - - subject with high stiffness from low compression; — - — subject with high stiffness from high compression

4.2. General frequency behaviour and inter-subject variability

The mean storage and loss moduli and the output stiffness $K_{dyn}^{Output}(\nu)$ averaging phase are shown in Fig. 9 for the following experimental set-up: a vibration excitation amplitude of 5 $m.s^{-2}$ *rms* and a quasi-static preloading equivalent to a static stiffness of 8 $N.mm^{-1}$. These parameters were selected because the obtained dynamic stiffness allows characterization of the dynamic behaviour of the distal phalanx very distinctly.

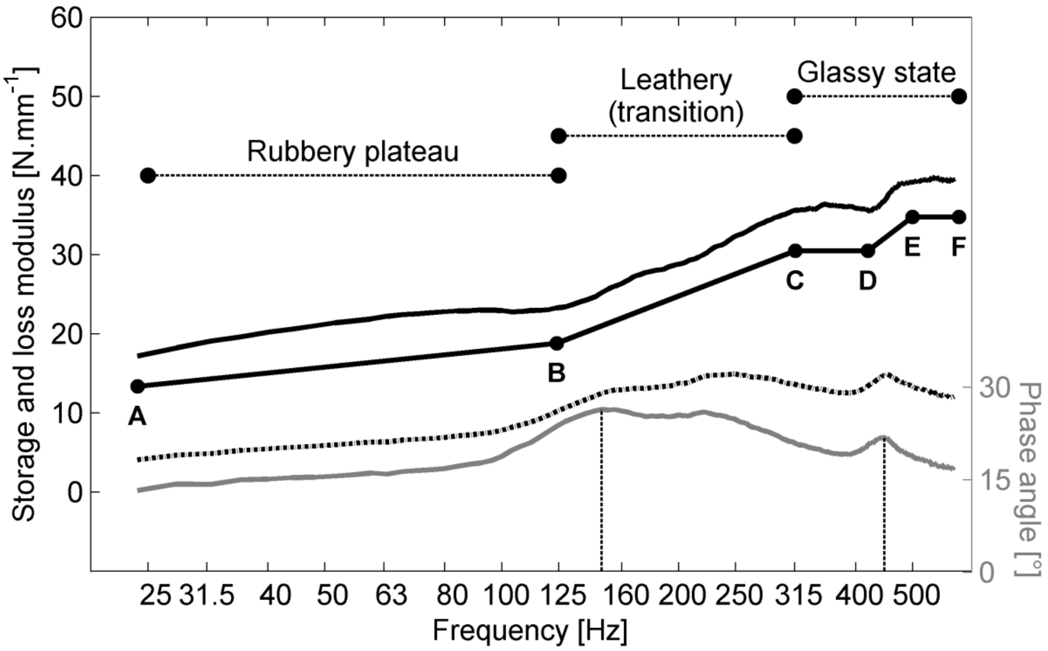

Fig. 9. Three basic ways to present the dynamic output stiffness for the experimental condition: acceleration 5 $m.s^{-2}$ *rms* and preload 8 $N.mm^{-1}$; the left axis is assigned to the stiffness modulus, the right axis to the phase angle; storage modulus; loss modulus; phase angle; linear interpolation of the storage modulus with an offset of -5 $N.mm^{-1}$ for better visualization.

Overall, the stiffness storage modulus increases continuously with frequency. The first phenomenon revealed is a stiffening of the distal phalanx as the vibration excitation frequency increases. The storage modulus increases from 16 $N.mm^{-1}$ at 25 Hz to 37 $N.mm^{-1}$ at 500 Hz. The distal phalanx is twice as stiff at 500 Hz as at 25 Hz. The real part of the stiffness exhibits three distinct frequency zones. The first zone exists between 25 and 125 Hz where the stiffness is approximately 20 $N.mm^{-1}$ and has moderate variation (the gradient is 2 $N.mm^{-1}$ per octave). The second zone lies between 125 and 315 Hz where the storage modulus increases quickly from 21 to 33 $N.mm^{-1}$ with an average gradient of 9 $N.mm^{-1}$ per octave. The third zone lies between 315 and 550 Hz (the spectral limit of our measurements), where the stiffness increases rapidly (the gradient is 16 $N.mm^{-1}$ per octave). The shapes of the stiffness curves in Fig. 9 are similar to those plotted using viscoanalyzer measurements for amorphous polymers (Menard, 2008 p. 26 and Lakes, 2009 p. 228). By analogy with rheology, the phalanx stiffness can be considered to be composed of a rubbery plateau of low stiffness up to 125 Hz, followed by a region of steep rise in stiffness between 125 and 315 Hz, called the glassy transition, and finally, a glassy state of higher stiffness (more than twice that of the rubbery plateau). The dynamic stiffness phase angle has two local maxima at 150 and 450 Hz that are associated with two points of inflection in the real part of the stiffness. In the field of rheology, the first local maximum is called the α peak or relaxation α and is associated with the point of inflection in the glassy transition zone. The second local maximum is called the β peak or relaxation β and is related to the point of inflection in the stiffness rise in the glassy state.

Input and output stiffnesses exhibit a rubbery plateau followed by a glassy transition zone before entering an ultimate glassy state (Fig. 10 (a) and (b)). Input and output storage moduli are very close up to a frequency of approximately 125 Hz (Fig. 10 (a)). Input and output rubbery plateaus are then quite similar. Above 125 Hz, the input storage modulus is less than the output modulus. Unlike the phase of the output stiffness, that of the input stiffness increases continuously up to 400 Hz where the relaxation β is distinct.

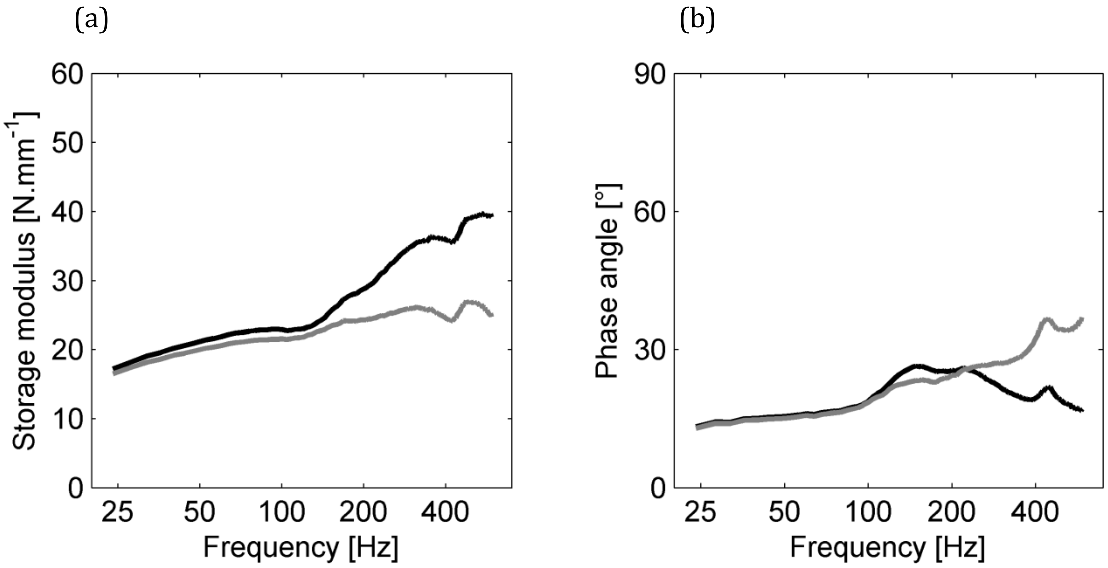

Fig. 10. Comparison of input and output dynamic stiffness for the following experimental conditions: acceleration 5 m.s^{-2} *rms* and preload 8 N.mm^{-1}; (a) storage modulus; (b) phase angle; storage modulus of input stiffness; storage modulus of output stiffness.

We quantified the inter-individual variation using the 95% confidence interval to gain an understanding of the output stiffness measurement dispersion. The mean output stiffness and 95% confidence interval are shown in Fig. 11 for the following experimental conditions: an acceleration level of 5 m.s^{-2} *rms* and a quasi-static preloading of 8 N.mm^{-1}. In this case, the half-width of the 95% confidence interval is 20%, and it has the same order of magnitude under all other experimental conditions.

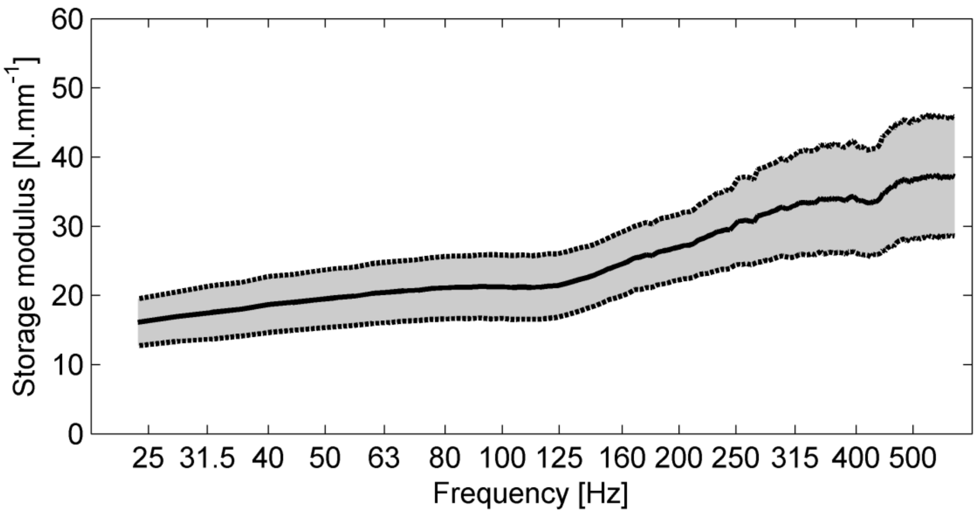

Fig. 11. Dispersion of the output storage modulus under the following experimental conditions: acceleration 5 m.s^{-2} *rms* and preloading 8 N.mm^{-1}; mean value; 95% confidence interval.

4.3. Acceleration power kernel

The acceleration power kernel is shown in Fig. 12 for the following conditions: acceleration level = 5 m.s^{-2} *rms* and quasi-static preloading = 8 N.mm^{-1}.

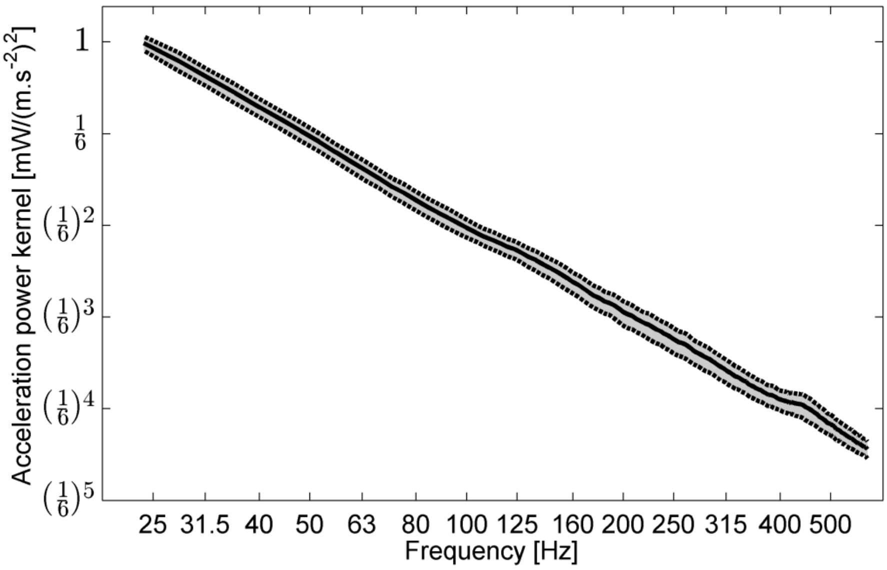

Fig. 12. Acceleration power kernel for experimental condition: acceleration 5 m.s^{-2} *rms* and preloading 8 N.mm^{-1}; mean value; 95% confidence interval.

The acceleration power kernel decreases quasi-linearly with respect to frequency. The interpolated straight line slopes at approximately -7.6 dB/octave. In other words, the acceleration power kernel (and hence, the dissipated power for harmonic excitation) is divided by six, when the frequency doubles. As described in Sections 4.4 and 4.5 of this paper, this behaviour is exhibited regardless of the excitation amplitude and static preloading. We can therefore establish the following empirical rule: when a phalanx is preloaded and harmonically vibrated by a cylindrical indenter (diameter: 7 mm) under iso-acceleration, doubling of the frequency leads to a six-fold reduction in the power dissipated by the distal phalanx.

When the vibration excitation is sinusoidal, the power dissipated by the distal phalanx is related to both the acceleration amplitude and frequency, as shown in Eq. (5). Based on this relation, iso-power dissipation charts can be plotted with respect to the *rms* sinusoidal acceleration level and its frequency. Examples of these charts are provided in Fig. 13. The acceleration power kernel used for plotting these charts corresponded to that of the following experimental condition: acceleration level = 5 m.s^{-2} *rms* and quasi-static preloading = 8 N.mm^{-1}. In the following sections, we show that this acceleration power kernel depends on the quasi-static preloading but depends weakly on excitation amplitude at frequencies below 80 Hz. Hence, these abacuses are suitable only above this frequency. Charts of the same type but different from those shown in Fig. 13 can be plotted for each static preloading.

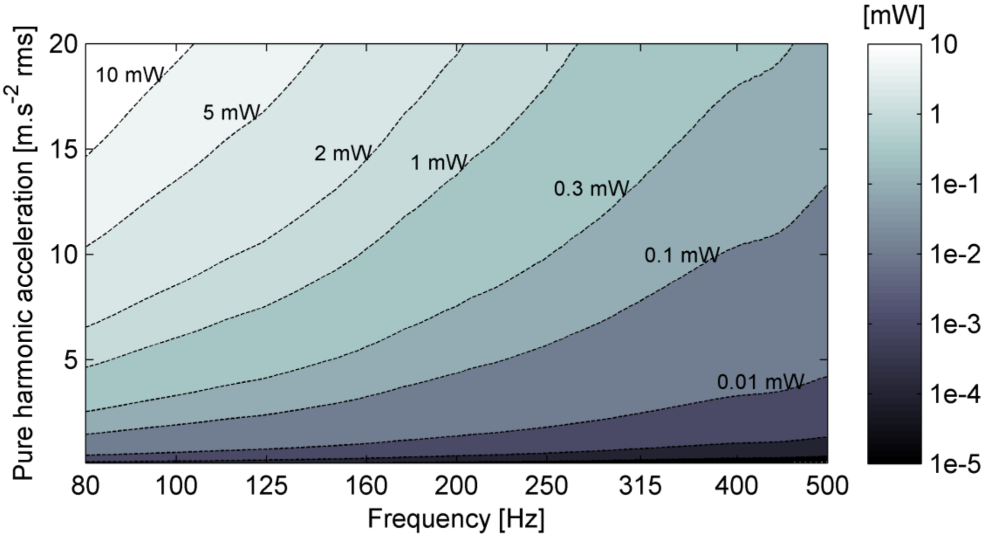

Fig. 13. Charts of dissipated iso-power under pure harmonic vibration for a preloading of 8 N·mm^{-1}. The dissipated power was computed from the acceleration power kernel based on the following experimental condition: acceleration 5 m.s^{-2} *rms* and preloading 8 N.mm^{-1}.

These charts are especially of interest because they provide an overall view of the dissipated power variation with respect to the acceleration level and frequency. They also enable quick selection of an acceleration level or frequency combination that yields the given dissipated power. For example, it is easy to find which acceleration level or frequency combination is associated with a dissipated power of less than 0.1 mW. Under the assumption that we can link vibration pathology development to a dissipated power threshold that must not be exceeded, such charts will enable us to select the threshold amplitude or frequency combinations for vibration-induced white finger pathology at frequencies higher than 80 Hz.

4.4. Effects of preloading for a fixed vibration level

The impact of the quasi-static preloading at a fixed acceleration level can be analysed with regard to the following four quantities: storage modulus, loss modulus, acceleration power kernel, and output stiffness phase angle. These four quantities are shown in Fig. 14 (a), (b), (c), and (d) for an acceleration level of 5 $m.s^{-2}$ *rms*.

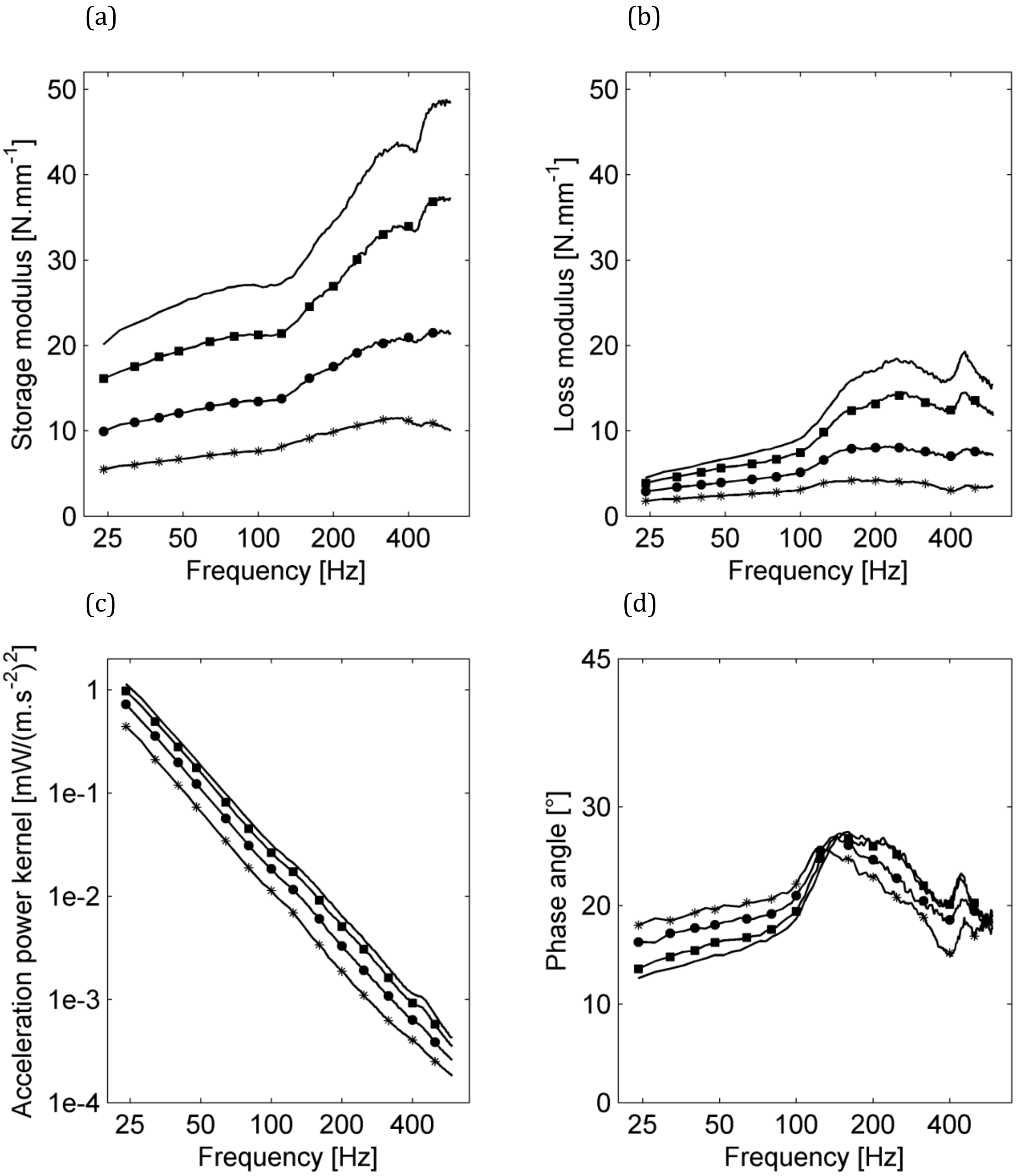

Fig. 14. Effects of preloading for a 5 m.s^{-2} *rms* vibration level; (a) output storage modulus; (b) output loss modulus; (c) acceleration power kernel; (d) phase angle of the output stiffness; —✱—2 N.mm^{-1}; —●—5 N.mm^{-1}; —■—8 N.mm^{-1};——10 N.mm^{-1}.

The effect of the static preloading on the storage and loss moduli is clearly shown in Fig. 14 (a) and (b). These moduli increase with the static preloading. The preloading influences for the rubbery plateau and the glassy transition zone are not identical. On the rubbery plateau, in addition to the overall increase in stiffness, when the preloading increases, the slope of the interpolated straight line on this plateau increases more moderately that that of the interpolated straight line in the glassy transition zone (an example of these straight lines is provided in Table 3 with the values of the gradients).

Table 3

Slope of the storage modulus on the rubbery plateau and in the glassy transition zone for various preloadings.

Quasi-static stiffness [$N.mm^{-1}$]		2	5	8	10
Slope [$N.mm^{-1}$ per octave]	Rubbery plateau	1	1.5	2	2.5
	Glassy transition	2	5	9	12

The consequence of an increase in preloading is, therefore, an overall rise in dynamic stiffness with more pronounced effects in the glassy transition frequency zone (the ratio of the slopes for the maximum and minimum preloadings is 6) than on the rubbery plateau (the corresponding ratio is 2.5). This synergy between frequency and static preloading was also confirmed by the results of a variance analysis test in which the frequency and preloading combined term had a p-value much less than 0.05. In addition to the increased stiffness, the loss modulus increases with increase in the preloading; in this case too, the effect is more pronounced in the glassy transition zone. As showed in Fig. 14 (c), the acceleration power kernel is small when the preloading is low. The decrease in the frequency of the acceleration power kernel remains virtually identical regardless of the level of quasi-static pre-load. There is no synergetic effect between the level of preloading and frequency. The acceleration power kernel curves are simply translated when the preloading varies (except at approximately 400 Hz, where the curves differ slightly). We quantified the relationship between the static preloading variation and the power dissipation variation under iso-acceleration. On average, over the frequency band, doubling the static preloading causes twice as much energy dissipation (this ratio varies between 1.8 and 2.3 over the spectral bandwidth). Moreover, the output stiffness phase angles shown in

Fig. 14 (d) exhibit two paradoxical effects of the static preloading on frequency mismatch in relaxations α and β: the lower the preloading, the lower are the frequencies of α and the higher are the frequencies of β. In other words, decreasing the static preloading effectively reduces the spectral bandwidth of the rubbery plateau and increases the bandwidth of the glassy transition zone, even when these variations are relatively low, especially in the case of β.

To gain a statistical understanding of the results, we plotted the mean storage and loss moduli and the corresponding lower and upper bounds of the 95% confidence interval in Fig. 15 (a) and (b). For both storage and loss moduli, the 95% confidence intervals are well separated for low static preload (2 $N.mm^{-1}$ and 5 $N.mm^{-1}$). In contrast, for higher static compressions (8 $N.mm^{-1}$ and 10 $N.mm^{-1}$), the 95% confidence intervals overlap. We also developed a general model for the analysis of variance (ANOVA) to determine the significance of the static preloads on the storage and loss moduli (differences were considered significant at the $p < 0.05$ level). Statistical analysis with the data from all subjects at a fixed vibration amplitude (here, 5 $m.s^{-2}$ *rms*) shows that both frequency ($p < 0.0001$) and static preload ($p < 0.0001$) are statistically significant factors for dynamic stiffness. Furthermore, there exists a statistically significant interaction between frequency and static preload ($p < 0.03$). In fact, as shown in Fig. 15 (a) and (b), beyond 125 Hz, the slope of the dynamic stiffness in the leathery state depends on both the compression level and frequency. In addition, a Tukey's honest significant difference (HSD) multiple comparison test was performed to determine the means of the storage and loss modulus that are significantly different from each other. We found that the means of storage and loss modulus for each compression rate are statistically significantly different from each of the other three. The statistical analyses for the acceleration power kernel and phase angle are not presented here because these two quantities are determined from storage and loss moduli, and hence, the same conclusions as those for the latter quantities can be drawn. To summarize, the higher the static preloading, the higher is the dynamic stiffness and the more intense is the vibration energy dissipation.

(a)

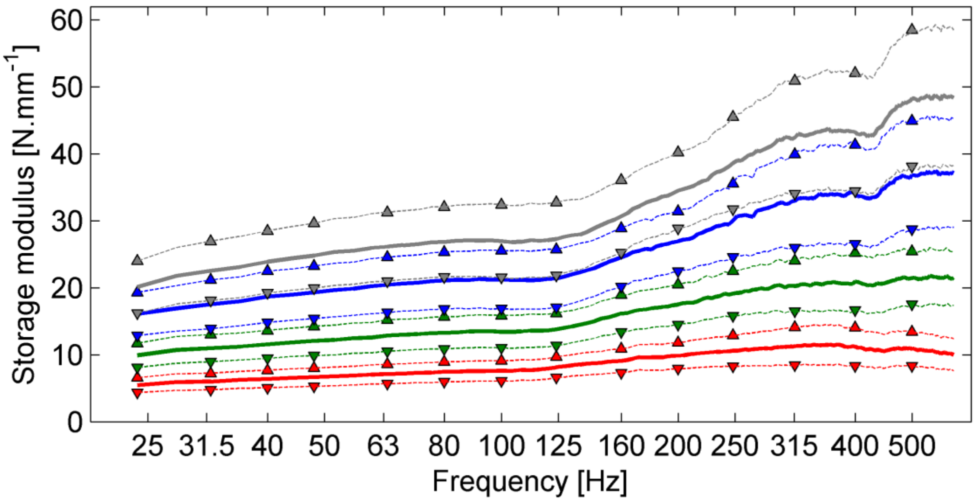

(b)

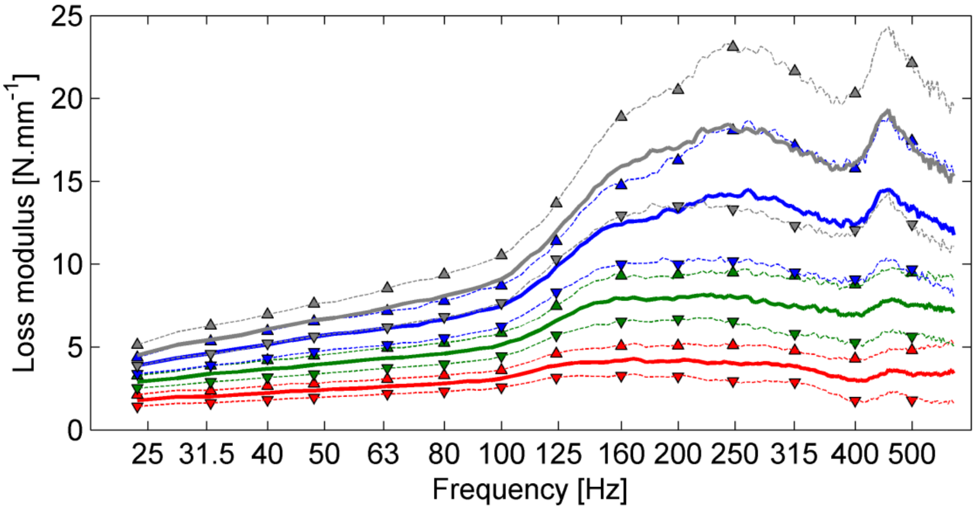

Fig. 15. Variability of subjects for a 5 m·s^{-2} *rms* vibration level; (a) output storage modulus; (b) output loss modulus; 2 N.mm^{-1}; 5 N.mm^{-1}; 8 N.mm^{-1}; 10 N.mm^{-1}; upper bound of the 95% confidence interval; lower bound of the 95% confidence interval.

4.5. Effects of the vibration level for a fixed preloading

The output stiffness loss moduli are shown in Fig. 16 for the four preloadings and five acceleration levels listed in Table 2.

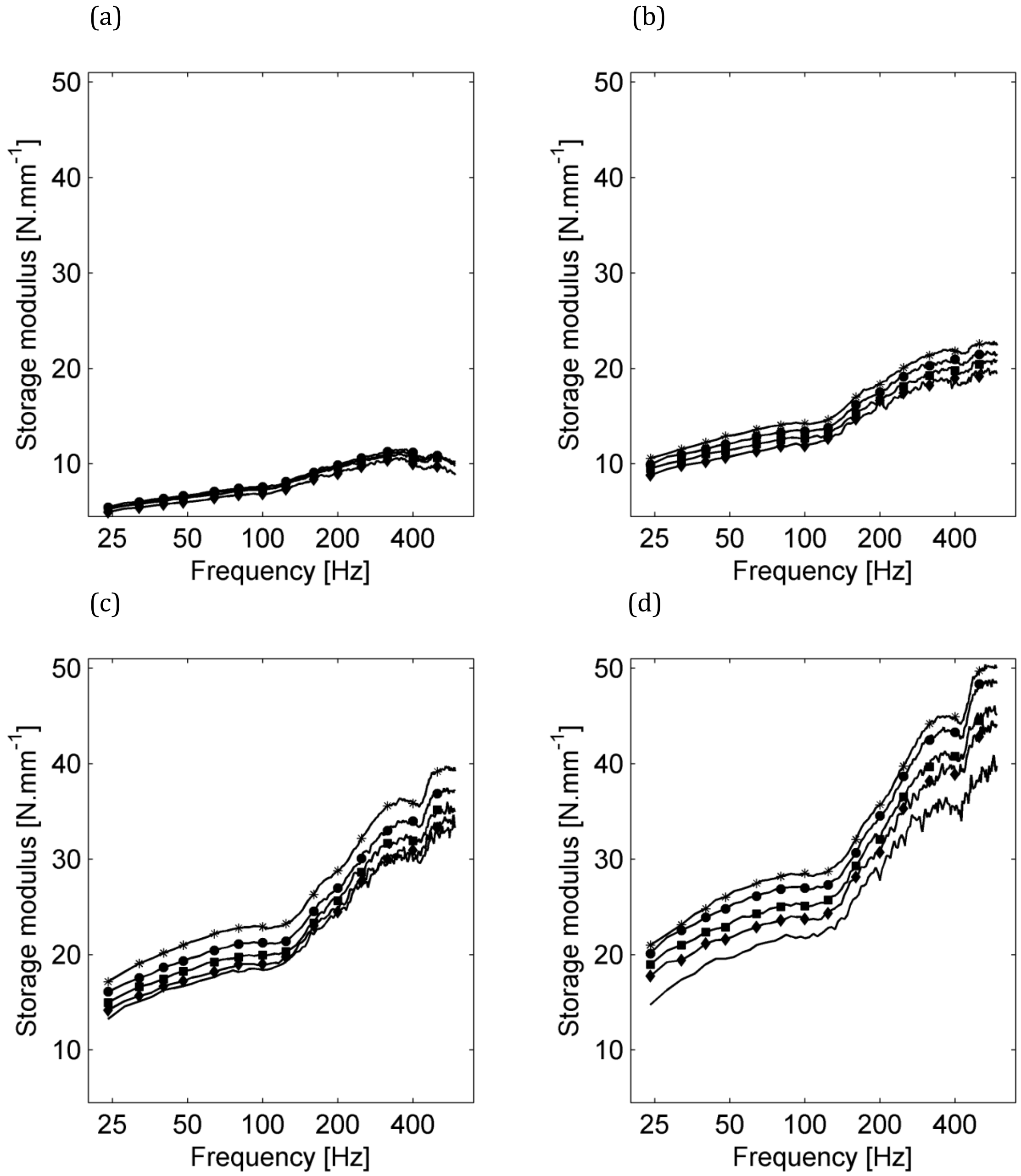

Fig. 16. Effects on changes in the storage modulus of a fixed preloading vibration level; preloading: (a) 2 N.mm^{-1}; (b) 5 N.mm^{-1}; (c) 8 N.mm^{-1}; (d) 10 N.mm^{-1}; —✱—2 m.s^{-2} *rms*; —●—5 m.s^{-2} *rms*; —■—10 m.s^{-2} *rms*; —◆—15 m.s^{-2} *rms*; ——20 m.s^{-2} *rms*.

For the two smallest preloadings (2 N.mm^{-1} and 5 N.mm^{-1}), only the first four acceleration amplitudes are plotted in Fig. 16 (a) and (b). This because when the excitation amplitude is 20 m.s^{-2} *rms*, the coherence between acceleration and force is too low, and the transfer function cannot be calculated accurately under such conditions. Fig. 16 (a) to (d) clearly show a decrease in the distal phalanx stiffness when the excitation amplitude increases. An analysis of variance highlighted that both frequency ($p < 0.0001$) and vibration amplitude ($p < 0.0003$) are statistically significant factors for the storage modulus. There is no synergic interaction between frequency and amplitude ($p > 1$). Indeed for each vibration amplitude, the storage moduli are simply translated (like an offset effect) without any modification of the shape of the associated curves. A Tukey's HSD test was performed to identify the amplitudes for which the means of the storage modulus are significantly different. It shows significant differences between the means of the storage modulus at high acceleration amplitudes and low levels. The results are listed in Table 4.

Table 4

Statistical multi-comparisons of the significant differences in the mean storage modulus for several vibration amplitudes; the grey cells indicate no significant differences, and the white cells indicate significant differences.

	2 m.s^{-2} *rms*	5 m.s^{-2} *rms*	10 m.s^{-2} *rms*	15 m.s^{-2} *rms*	20 m.s^{-2} *rms*
2 m.s^{-2} *rms*					
5 m.s^{-2} *rms*					
10 m.s^{-2} *rms*					
15 m.s^{-2} *rms*					
20 m.s^{-2} *rms*					

Fig. 17 (a), (b), (c), and (d) (both linear and logarithmic scales were used) show that the variation in vibration excitation amplitude has an insignificant influence on the acceleration power kernel for all frequencies for 2 N.mm^{-1} and 5 N.mm^{-1} preloadings and above 80 Hz for 8 N.mm^{-1} and 10 N.mm^{-1} preloadings. The acceleration excitation amplitude affects distal phalanx softening or stiffening, but has limited influence on the dissipated vibration power kernel at high frequencies (>80 Hz). In other words, at high frequencies (>80 Hz), the input vibration amplitude does not intrinsically affect the dissipation of the mechanical power of the phalanx regardless of the compression. At low frequencies, the input vibration amplitude has a small effect only for large preloadings.

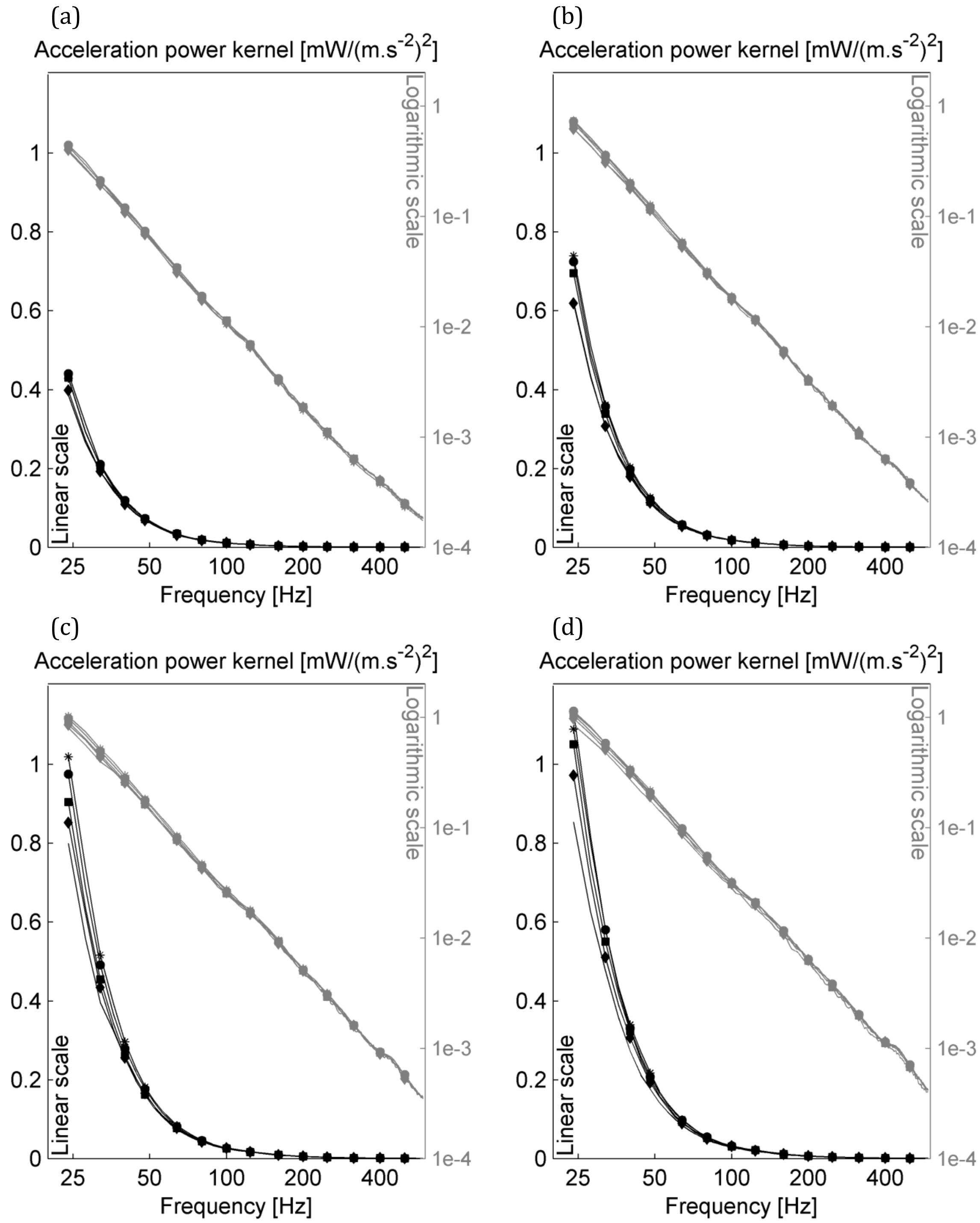

Fig. 17. Effects of a fixed preloading vibration level on acceleration power kernel; preloading: (a) 2 N.mm^{-1}; (b) 5 N.mm^{-1}; (c) 8 N.mm^{-1}; (d) 10 N.mm^{-1}; 2 m.s^{-2} *rms*; 5 m.s^{-2} *rms*; 10 m.s^{-2} *rms*; 15 m.s^{-2} *rms*; 20 m.s^{-2} *rms*.

5. Discussions

5.1. Main potential measurement errors

When measuring the output force, the fingertip is placed on a steel shell support. The weight of this phalanx support (11 g) was added to that of the top seismic mass of the piezoelectric element, thereby reducing the resonance frequency of the sensor. However, by using the sensor characteristics in its data sheet and by assuming a mechanical second-order system behaviour, we theoretically found that the modified resonance frequency (>10 kHz) remained much higher than the maximum frequency of the spectral band considered in our study. Hence, the weight added by the phalanx support caused little disturbance in the output force measurements. Furthermore, the impedance of the foundation on which the force sensor is fixed can lead to discrepancies between the true and measured forces if it is not considered in the force assessment (Braender, 1972). However, in the case of a very heavy foundation (i.e. very low foundation velocity), the measurement error becomes insignificant except near the resonant frequency of the sensor. For each measurement, we conducted a check with the control accelerometer (Fig. 1 item b) placed near the force sensor to ensure that the foundation velocity remains negligible.

With regard to the static stiffness assessment, both the fingertip compression i.e. the cylindrical probe displacement and the output static force should be accurately estimated. However, phalanx compression may be inaccurate if the just-in-contact condition between the probe and phalanx is improperly evaluated. Indeed, the probe displacement should be measured with reference to the position at which the indenter and phalanx barely touch in order to prevent initial deformation of the phalanx, which can cause a measurement error. Given the very low stiffness of soft tissues with respect to minor compressions, the just-in-contact condition is extremely difficult to estimate and reproduce by the experimenter. Therefore, a simple electronic system that operates at very low currents (<2 mA, which is safe for humans) was developed. When the indenter makes contact with the distal phalanx, an electroluminescent diode lights up.

Assessing the quasi-static effort with a piezoelectric sensor is a great challenge. Actually, the measuring system only provided an estimate of the DC component of the force response because of both the metrological limitations caused by the combination of the charge amplifier and piezoelectric sensor and the physical stress relaxation phenomena. The stresses measured dynamically at a given moment were different from those obtained under quasi-static conditions (Wu et al., 2003). Forces were measured at a low loading speed to minimize viscous effects. Conversely, if the measuring time increases, the electronic discharge process (low frequency limitation) and charge amplifier output voltage drift (zero drift) strongly disrupt the force measurement (Gatti and Ferrari, 1999). The final measuring time reflects a balance between the discharge time constant (100 s), charge amplifier output voltage drift (no effect if the measurement time is less than 20 s), and relaxation effect (weak if the measuring time exceeds 10 s based on phalanx tests). Based on a large number of measurements synthesised in the technical report (Noel, 2015), we concluded that if the measuring time is between 10 s to 15 s, the relative error between true static force and the quasi-static force measured with the piezoelectric force output sensor is less than 10%. This is in good agreement with the results of the validation tests as indicated by comparison with a reference compression test machine (Section 2.5). The measuring time selected was, therefore, between 10 s and 15 s.

Moreover, the aluminium disc with the telemeter for displacement measurement, the screw for fixing the impedance head, the cylindrical probe, and the fingertip support were designed such that their first resonance frequencies were much higher than the upper limit of the spectral range analysed in this study. This ensured that no noise was transmitted by these elements to the fingertip because the measured coherence functions between the different mechanical quantities were almost unity.

5.2. Rheological standpoint and physiological analogy

The dynamic stiffnesses of the distal phalanxes exhibit similar behaviour as those of the measured stiffnesses of certain elastomers (Fig 9). This indicates that the macromolecular structure of the conjunctive tissues of the distal phalanx is likely similar to that of amorphous polymers. More specifically, the viscoelastic properties of distal phalanxes are mainly induced by the extracellular matrix of the conjunctive tissues (Vicente, 2012). These tissues occupy the space between the cells, nourish, and support the cells. These tissues are composed of a complex network of macromolecules that can be grouped into three main types (Callen and Perasso, 2005 p. 432-443): i) very voluminous fibrous proteins, i.e. collagen and elastin; ii) less voluminous glycoproteins that ensure the adhesion of the different matrix constituents with the cells or among themselves; and iii) complex carbohydrates (polysaccharides) and glycosaminoglycans that are often attached to a protein to form proteoglycans. They form a hydrated gel that fills the water-retaining matrix. The adhesive glycoproteins and polysaccharides form a gel substance called the ground substance. The most important polysaccharide in the ground substance of the distal phalanx is hyaluronic acid (Feng and Lu, 2011; Vicente, 2012). The hyaluronic acid chains have secondary proteoglycan chains (the versican in the dermis: a special type of proteoglycan) that are linked by adhesion glycoproteins to the constituents of the extracellular matrix, such as collagen and elastin. Because of this complex assembly of macromolecules, the distal phalanxes exhibit a viscoelastic behaviour similar to that of elastomers. The vibration energy dissipation properties are therefore explained (Purslow et al., 1998; Shen et al., 2011) either by molecular rearrangements of different components of the extracellular matrix (more specifically in the collagen and ground substance) or by movements that cause viscous shear forces between the fluid (ground substance) and solid (collagen and elastin) phases.

The softening phenomenon related to an increase in the excitation amplitude (Fig. 16) is known in certain amorphous polymers, especially those with large carbon black content.

The phenomenon is called the Payne effect or the Fletcher–Gent effect. This dependence of distal phalanx stiffness on the vibration excitation amplitude can be considered in the context of the thixotropic nature of the ground substance (Feng and Lu, 2011 p.14). The ground substance effectively has the consistency of a gel with the two defining properties of thixotropy (Barnes, 1997): i) the gel is rheofluidifying (shear rate thinning), i.e. its viscosity decreases with increasing mechanical stress. In other words, this gel behaves more as a solid at low stresses and more as a fluid at higher stresses. The macroscopic consequence of this characteristic may be a reduction in stiffness under increased amplitude (relaxation associated with a more fluid nature of the ground substance at high stresses). ii) the effects of this fluidification are not out of phase with stress application, but occur later. Similar to viscoelasticity, this behaviour reflects the dissipative nature of the ground substance.

5.3. Physical interpretation of results and comparison with other works

A number of works (Reynolds and Angevine, 1977; Sörensson and Lundström, 1992; Wu et al., 2006) have highlighted that low-frequency vibrations can propagate from the fingers to the whole hand-arm system, while high-frequency vibrations (>100 Hz) are more localized in the finger contact area because of the mechanical damping abilities of soft tissues (Wu et al., 2006). Hence, findings may be compared in terms of the trend of high-frequency vibrations, regardless of the test methods even if some differences are present. Thus, our results may be considered either from the perspective of local finger biodynamic responses or the responses distributed in the hand-finger system.

The biodynamic response of the fingertip is expected to be controlled by the tissue elasticity up to a frequency of approximately 125 Hz (almost constant stiffness—segment [AB] Fig. 9—with a phase less than 15°). The same behaviour was observed in a number of studies where the frequency of slope failure (point B Fig. 9) varied between 100 Hz and 200 Hz. In Lundström's study (Lundström, 1984), this frequency is approximately 200 Hz, while it is approximately 100 Hz for Kern and Werthschützky (Kern and Werthschützky, 2008), Mann and Griffin (Mann and Griffin, 1996), and Wiertlewski and Hayward (Wiertlewski and Hayward, 2012) and 130 Hz for Moore and Mundie (Moore and Mundie, 1972; Moore, 1970). The latter two studies highlighted that the failure frequency at 130 Hz occurs not only at the fingertip, but also in the thenar eminence, the volar forearm, and the thigh. This observation led to the hypothesis that this failure frequency is not specific to the finger but is related to the mechanical behaviour of the human skin. Dong and co-workers (Dong et al., 2004c) reported a stiffening of the fingers biodynamic response as measured with an instrument handle at approximately 80 Hz. The leathery transition (segment [BC] Fig. 9) and the glassy state (segments [CD,EF] Fig. 9) were not emphasized by Lundström (Lundström, 1984), but Wu and co-workers (Wu et al., 2006) found some inconsistency in Lundström's measurements at high frequencies. However, the leathery and glassy states were thoroughly measured by Moore and Mundie (Moore and Mundie, 1972) who found the glassy state at approximately 400 Hz, which is in good agreement with our findings. Dong and co-workers (Dong et al., 2004c) also reported changes in the dynamic response at 300 Hz and 500 Hz. On a separate note, Liang and Boppart (Liang and Boppart, 2010) measured the Young's modulus of the human skin in the palm and forearm by using dynamic optical coherence elastography. They concluded that the Young's modulus of the skin is almost constant between 100 Hz and 200 Hz, and then increases up to 300 Hz and remains constant up to 400 Hz, beyond which, it rises again. This material behaviour is very similar to those of the storage modulus measured in this study.

Output and input stiffnesses differ from 125 Hz (Fig. 10). Indeed, the input stiffness is mainly controlled by the soft tissues of the fingertip, whereas the output stiffness is influenced by stiffer anatomical elements such as the bone and the nail (because of measurement localisation). Similarly, the input stiffness phase angle is greater than the output stiffness phase angle because the bones and the nails have less damping ability than the soft tissues.

The effect of the static preloading on biodynamic responses was studied by Lundström (Lundström, 1984) who found a slight increase in the dynamic stiffness with doubling of the pre-stress, but the preloading level considered in the previous study was much less than that in the present study. In the study of Moore and Mundie (Moore and Mundie, 1972), the preloading was only significant for frequencies less than 130 Hz, whereas in the high-frequency region, the effect of static loads was measured. However, Dong and co-workers (Dong et al., 2004c) and Kern and Werthschützky (Kern and Werthschützky, 2008) found that the gripping forces or static loads have considerable effects, but they do not cause dissimilar behaviour between the rubbery plateau and the leathery or glassy state, as we found in the present work. However, the boundary conditions of the fingers in their works were different from those in our study. Their works incorporated inertial effects largely, and this may be the cause of the observed differences.

Lundström (Lundström, 1984) studied the effects of input acceleration amplitude on biodynamic responses. He found that the input acceleration amplitude exerts an influence only in low-frequency (<100 Hz) region; however, for the same reason as explained earlier, no definitive conclusions can be draw at high frequencies. In the study of Gurram and co-workers (Gurram et al., 1995), the input acceleration amplitudes do not modify the hand-arm-system biodynamic response regardless of the frequency range. On the other hand, Marcotte and co-workers (Marcotte et al., 2005) found that the level of input acceleration could change the mechanical impedance at low frequencies only (<100 Hz). In the present study, we showed that the input acceleration amplitude may have a major influence on the storage modulus at all frequencies. We further showed that it affects the dissipated mechanical power slightly only at low frequencies (<50 Hz).

6. Conclusions

In this study, an experimental apparatus was built for measuring static and dynamic stiffnesses in preloaded distal phalanxes. The experimental set-up and test bench were validated by comparing their results with those obtained using a tension-compression machine and a viscoanalyzer. Twenty subjects participated in the test, to provide the statistical data representative of an average index finger. Analysis of the measured dynamic stiffnesses highlighted that the phalanx exhibited mechanical behaviour similar to that of certain amorphous polymers. The phalanx stiffnesses in fact increase with the vibration frequency, exhibiting a rubbery plateau, a glassy transition zone, and a glassy state. Under iso-excitation amplitude and iso-static preloading, the power dissipated in the phalanx is divided by six when the frequency is doubled. The influence of the static preloading and vibration excitation amplitude was subsequently investigated. The higher the preloading state, the higher is the dynamic stiffness with a very pronounced frequency and preloading synergy effect below 125 Hz. The dissipated power is also affected by the level of preloading because doubling this level leads to twice as much vibration dissipation. Additionally, an increase in vibration excitation amplitude causes a decrease in the phalanx stiffness, similar to the Payne effect or the Fletcher–Gent effect encountered in a number of rubbers. The thixotropic nature of the extracellular matrix may be the cause of this decrease in phalanx stiffness. Our measurements also revealed that the acceleration power kernel was not influenced by the vibration excitation level at high frequencies (clearly, the dissipated power is directly linked to the vibration amplitude). Using these kernels, the iso-dissipated power charts were plotted for each static preloading and were used for selecting the frequency and amplitude combinations to realize a target dissipated power. These experimental results will be used for adjusting and validating finite element models of preloaded, vibrated phalanxes.

Acknowledgements

The author would like to thank his INRS colleagues, who actively participated in the work described in this paper: Dr. Jean-Pierre Meyer (research physician), Isabelle Manet, Dominique Bruant, Alexandre Klingler, and Richard Poirot.

References

Adewusi, S.A., Rakheja, S., Marcotte, P., Boileau, P.-E., 2008. On the discrepancies in the reported human hand–arm impedance at higher frequencies. Int. J. Ind. Ergon. 38, 703–714. doi:10.1016/j.ergon.2007.12.004

Aldien, Y., Marcotte, P., Rakheja, S., Boileau, P.-E., 2006. Influence of hand–arm posture on biodynamic response of the human hand–arm exposed to zh-axis vibration. Int. J. Ind. Ergon. 36, 45–59. doi:10.1016/j.ergon.2005.07.001

Åström, C., Rehn, B., Lundström, R., Nilsson, T., Burström, L., Sundelin, G., 2006. Hand-arm vibration syndrome (HAVS) and musculoskeletal symptoms in the neck and the upper limbs in professional drivers of terrain vehicles-A cross sectional study. Appl. Ergon. 37, 793–799. doi:10.1016/j.apergo.2005.09.004

Barnes, H.A., 1997. Thixotropy - A review. J. Nonnewton. Fluid Mech. 70, 1–33. doi:10.1016/S0377-0257(97)00004-9

Besa, A.J., Valero, F.J., Suñer, J.L., Carballeira, J., 2007. Characterisation of the mechanical impedance of the human hand–arm system: The influence of vibration direction, hand–arm posture and muscle tension. Int. J. Ind. Ergon. 37, 225–231. doi:10.1016/j.ergon.2006.10.019

Bovenzi, M., 1990. Medical aspects of the Hand -Arm vibration syndrome. Int. J. Ind. Ergon. 6, 61–73.

Braender, W., 1972. High-Frequency-Response to Force-Transducers. B&K Tech. Rev. 3, 15–22.

Burström, L., 1997. The influence of biodynamic factors on the mechanical impedance of the hand and arm. Int. Arch. Occup. Environ. Health 69, 437–446. doi:10.1007/s004200050172

Burström, L., Lundstrom, R., 1998. Comparison of different measures for hand – arm vibration exposure. Saf. Sci. 28, 3–14.

Callen, J.C., Perasso, R., 2005. Biologie cellulaire - 2ème édition - Des molécules aux organismes, Sciences de la vie. Dunod, Paris.

Chai-Yu, F., Oliver, M., 2005. Direct Measurement of Index Finger Mechanical Impedance at Low Force. First Jt. Eurohaptics Conf. Symp. Haptic Interfaces Virtual Environ. Teleoperator Syst. 1, 657–659. doi:10.1109/WHC.2005.40

Chetter, I.C., Kent, P.J., Kester, R.C., 1997. The hand arm vibration syndrome: A review. Cardiovasc. Surg. 6, 1–9. doi:10.1016/S0967-2109(97)00090-2

Dong, R.G., Schopper, a W., McDowell, T.W., Welcome, D.E., Wu, J.Z., Smutz, W.P., Warren, C., Rakheja, S., 2004a. Vibration energy absorption (VEA) in human fingers-hand-arm system. Med. Eng. Phys. 26, 483–492. doi:10.1016/j.medengphy.2004.02.003

Dong, R.G., Warren, C., Welcome, D., McDowell, T., Wu, J., 2004b. A comparison and evaluation of the reported mechanical impedance data of the human hand–arm system, in: 10th International Conference on Hand–arm Vibration. Las Vegas, pp. 221–227.

Dong, R.G., Welcome, D.E., McDowell, T.W., Wu, J.Z., 2008a. Analysis of handle dynamics-induced errors in hand biodynamic measurements. J. Sound Vib. 318, 1313–1333. doi:10.1016/j.jsv.2008.04.038

Dong, R.G., Welcome, D.E., McDowell, T.W., Wu, J.Z., 2004c. Biodynamic response of human fingers in a power grip subjected to a random vibration. J. Biomech. Eng. 126, 447–457. doi:10.1115/1.1784479

Dong, R.G., Welcome, D.E., McDowell, T.W., Wu, J.Z., Schopper, A.W., 2006. Frequency weighting derived from power absorption of fingers-hand-arm system under z(h)-axis vibration. J. Biomech. 39, 2311–2324. doi:10.1016/j.jbiomech.2005.07.028

Dong, R.G., Welcome, D.E., Wu, J.Z., 2005a. Frequency Weightings Based on Biodynamics of Fingers-Hand-Arm System. Ind. Health 5349, 516–526.

Dong, R.G., Wu, J.Z., McDowell, T.W., Welcome, D.E., Schopper, a W., 2005b. Distribution of mechanical impedance at the fingers and the palm of the human hand. J. Biomech. 38, 1165–75. doi:10.1016/j.jbiomech.2004.05.021

Dong, R.G., Wu, J.Z., Welcome, D.E., 2005c. Recent Advances in Biodynamics of Human Hand-Arm System. Ind. Health 43, 449–471. doi:10.2486/indhealth.43.449

Dong, R.G., Wu, J.Z., Welcome, D.E., McDowell, T.W., 2008b. A discussion on comparing alternative vibration measures with frequency-weighted accelerations defined in ISO standards. J. Sound Vib. 317, 1042–1050. doi:10.1016/j.jsv.2008.03.028

Feng, X., Lu, T., 2011. Introduction to skin biothermomechanics and thermal pain. Springer-Verlag, Berlin Heidelberg.

Gatti, P.L., Ferrari, V., 1999. Applied structural and mechanical vibrations - theory, methods and measuring instrumentation. E & FN Spon, London.

Griffin, M.J., 2012. Frequency-dependence of Psychophysical and Physiological Responses to Hand-transmitted Vibration. Ind. Health 50, 354–369. doi:10.2486/indhealth.MS1379

Griffin, M.J., 1996. Handbook of human vibration. Elsivier Academic Press, London.

Gulati, R.J., Srinivasan, M.A., 1997. Determination of mechanical properties of the human fingerpad in vivo using a tactile stimulator. Massachusetts Institute of Technology, Cambridge.

Gurram, R., Rakheja, S., Gouw, G.J., 1995. Mechanical impedance of the human hand-arm system subject to sinusoidal and stochastic excitations. Int. J. Ind. Ergon. 16, 135–145.

Hajian, a Z., Howe, R.D., 1997. Identification of the mechanical impedance at the human finger tip. J. Biomech. Eng. 119, 109–114. doi:10.1115/1.2796052

Håkansson, B., Carlsson, P., 1987. Bias errors in mechanical impedance data obtained with impedance heads. J. Sound Vib. 113, 173–183. doi:10.1016/S0022-460X(87)81349-4

ISO 5349-1:2001, 2001. Mechanical vibration -- Measurement and evaluation of human exposure to hand-transmitted vibration -- Part 1: General requirements.

Kattel, B.P., Fernandez, J.E., 1999. The effects of rivet guns on hand-arm vibration. Int. J. Ind. Ergon. 23, 595–608. doi:10.1016/S0169-8141(98)00074-2

Kern, T.A., Werthschützky, R., 2008. Studies of the Mechanical Impedance of the Index Finger in Multiple Dimensions, in: Ferre, M. (Ed.), Haptics: Perception, Devices and Scenarios: 6th International Conference, EuroHaptics 2008 Madrid, Spain, June 10-13, 2008 Proceedings. Springer Berlin Heidelberg, Berlin, Heidelberg, pp. 175–180. doi:10.1007/978-3-540-69057-3_21

Krajnak, K., Riley, D., Wu, J., Mcdowell, T., Welcome, D.E., Xu, X.S., Dong, R.G., 2012. Frequency-dependent Effects of Vibration on Physiological Systems: Experiments with Animals and other Human Surrogates. Ind. Health 50, 343–353. doi:10.2486/indhealth.MS1378

Lakes, R., 2009. Viscoelastic Materials, Nature. Cambridge University Press, New York.

Liang, X., Boppart, S. a., 2010. Biomechanical properties of in vivo human skin from dynamic optical coherence elastography. IEEE Trans. Biomed. Eng. 57, 953–959.

doi:10.1109/TBME.2009.2033464

Lundström, R., 1984. Local vibrations-mechanical impedance human hand's glabrous skin. J. Biomech. 1, 137–144.

Lundström, R., Burström, L., 1989. Mechanical impedance of the human hand-arm system. Int. J. Ind. Ergon. 3, 235–242. doi:10.1016/0169-8141(89)90023-1

Mann, N.A., Griffin, M.J., 1996. Effect of contact conditions on the mechanical impedance of the finger. Cent. Eur. J. Public Health 4, 46–49.

Marcotte, P., Aldien, Y., Boileau, P.-É., Rakheja, S., Boutin, J., 2005. Effect of handle size and hand–handle contact force on the biodynamic response of the hand–arm system under zh-axis vibration. J. Sound Vib. 283, 1071–1091. doi:10.1016/j.jsv.2004.06.007

Matoba, T., 1994. Pathophysiology and clinical picture of hand-arm vibration syndrome in Japanese workers. Nagoya J. Med. Sci. 57 Suppl, 19–26.

Menard, K.P., 2008. Dynamic Mechanical Analysis - A Practical Introduction, 2nd ed. CRC Press, Boca Raton.

Moore, T., Mundie, J., 1972. Measurement of Specific Mechanical Impedance of the Skin: Effects of Static Force, Site of Stimulation, Area of Probe, and and Presence of a Surround. J. Acoust. Soc. Am. 4, 577–584.

Moore, T.J., 1970. A Survey of the Mechanical Characteristics of Skin and Tissue in Response to Vibratory Stimulation. IEEE Trans. Man-Machine Syst. 11, 79–84. doi:10.1109/TMMS.1970.299966

Narini, P.P., Novak, C.B., Mackinnon, S.E., Coulson-Roos, C., 1993. Occupational exposure to hand vibration in northern Ontario gold miners. J. Hand Surg. Am. 18, 1051–1058. doi:10.1016/0363-5023(93)90402-O

Noel, C., 2015. Une stratégie de modélisation multi-échelles pour la prédiction de certains effets des vibrations sur le réseau vasculaire digital. INRS, Note scientifique & technique, NS 339.

Noel, C., 2011. Acceleration mapping and local biodynamic response of hand gripping a vibrating handle by using laser scanning vibrometer, in: 46th UK Conference on Human Response to Vibration. pp. 173–184.

Norcross, S.G., 2009. Evaluation and alternative regularization of audio equalization techniques. PhD Thesis, University of Ottawa.

Purslow, P.P., Wess, T.J., Hukins, D.W., 1998. Collagen orientation and molecular spacing during creep and stress-relaxation in soft connective tissues. J. Exp. Biol. 201, 135–142.

Reynolds, D.D., Angevine, E.N., 1977. Hand-Arm Vibration, Part 2: Vibration Transmission Characteristics of the Hand and Arm. J. Sound Vib. 51, 255–265.

Riande, E., Diaz-calleja, R., Prolongo, M.G., Masegosa, R.M., Salom, C., 2000. Polymer viscoelasticity, stress and strain in practice. New York.

Serina, E.R., Mote, C.D., Rempel, D., 1997. Force response of the fingertip pulp to repeated compression—Effects of loading rate, loading angle and anthropometry. J. Biomech. 30, 1035–1040. doi:10.1016/S0021-9290(97)00065-1

Shen, Z.L., Kahn, H., Ballarini, R., Eppell, S.J., 2011. Viscoelastic properties of isolated collagen fibrils. Biophys. J. 100, 3008–3015. doi:10.1016/j.bpj.2011.04.052

Sörensson, A., Lundström, R., 1992. Transmission of Vibration to the Hand. J. Low Freq. Noise Vib. 11, 14–22.

Vicente, J. de, 2012. Viscoelasticity – From Theory to Biological Applications. InTech, Rijeka.

Wiertlewski, M., Hayward, V., 2012. Mechanical behavior of the fingertip in the range of frequencies and displacements relevant to touch. J. Biomech. 45, 1869–1874. doi:10.1016/j.jbiomech.2012.05.045

Wu, J.Z., Dong, R.G., Smutz, W.P., Rakheja, S., 2003. Dynamic interaction between a fingerpad and a flat surface: experiments and analysis. Med. Eng. Phys. 25, 397–406. doi:10.1016/S1350-4533(03)00035-3

Wu, J.Z., Dong, R.G., Welcome, D.E., 2006. Analysis of the point mechanical impedance of fingerpad in vibration. Med. Eng. Phys. 28, 816–826. doi:10.1016/j.medengphy.2005.11.013